Equivalent-Charge-Based Optimization of Spokes-and-Hub Permanent Magnets for Hand-Held MR Imaging

by

Irene A. Kuang

B.S. Biomedical Engineering, The University of Texas at Austin (2017)

Submitted to the Department of Electrical Engineering and Computer Science
in partial fulfillment of the requirements for the degree of

Master of Science in Electrical Engineering and Computer Science

at the

MASSACHUSETTS INSTITUTE OF TECHNOLOGY

May 2020

© Massachusetts Institute of Technology 2020. All rights reserved.

Author . . . .
Department of Electrical Engineering and Computer Science
May 15, 2020

Certified by. . . . .
Jacob K. White
Professor of Electrical Engineering and Computer Science
Thesis Supervisor

Accepted by . . . .
Leslie A. Kolodziejski
Professor of Electrical Engineering and Computer Science
Chair, Department Committee on Graduate Students

Equivalent-Charge-Based Optimization of Spokes-and-Hub Permanent Magnets for Hand-Held MR Imaging

by

Irene A. Kuang

Submitted to the Department of Electrical Engineering and Computer Science
on May 15, 2020, in partial fulfillment of the
requirements for the degree of
Master of Science in Electrical Engineering and Computer Science

Abstract

The complex infrastructure needed for high-field magnetic resonance (MR) scanners has relegated this very safe, and remarkably revealing, clinical tool to high-end hospital care. But for many potential applications of MR—point-of-care diagnostics, routine screening or classroom experimentation—image quality is far less critical than portability and low cost. Emphasizing cost and portability over image quality has led researchers to focus on low-field MR, of the order of tens to hundreds of millitesla, generated using arrays of inexpensive permanent magnets. In this thesis, I describe a method for differentiating the potential from end-cap equivalent charges to efficiently compute the fields from bar magnets in a hundred- bar "spokes-and-hub" permanent magnet topology and demonstrate its potential as a low-cost MR imager.

Thesis Supervisor: Jacob K. White
Title: Professor of Electrical Engineering and Computer Science

Acknowledgments

I would like to thank my thesis advisor, Professor Jacob White, for his endless patience, vision, teachings, and willingness to spend many long hours in the lab with me. It's truly a pleasure to work with someone so enthusiastic about research and teaching.

Many thanks go out to all of my lab mates and the rest of the MR community of MIT and the Martino's Center. Thank you to Nick Arango, Georgy Guryev, Brandon Motes, Jason Stockmann, Patrick McDaniel, and Larry Wald for being people I could always rely on them for helpful discussion and advice. A very special thank you to Professor Elfar Adalsteinsson for introducing me to Jacob and the field of MR. Thanks also to Chadwick Collins and Megumi Masuda-Loos for all their administrative help and support.

None of this would be possible without the A4 Café, Mamaleh's Delicatessen, and Felipe's Taqueria for their unfailing support (and caffeine supply) throughout the process of researching and writing this thesis. I also owe my sanity to my friends both here at MIT and those many miles away – Alex Barksdale, Andrea Dillon, Annalisa Taylor, Ankita Ghoshal, Becki Ho, Chloe Wu, ChoongSze Lee, Elizabeth Shih, Gina Lee, Jason Zhang, Joseph Maalouf, Kristin Astrachan, Lucy Chai, Luis Limon III, Monica Agrawal, Nicholas Possis, Baby Sarah Wu, and Shankara Anand, to name a few.

Finally, I would like to express my deepest appreciation for my parents, JB and Sumin, and brothers, Matthew and Joe Joe, for supporting me through everything.

Contents

1 Introduction **13**

1.1 Low-Cost, Portable MRI 13

2 MRI Background **17**

2.1 Main Magnetic Field (B_0) 18

2.2 Radiofrequency (RF) Excitation (B_1) 18

2.3 Gradient Fields 19

2.4 Signal Acquisition 20

2.4.1 Projection-Based Reconstruction 20

2.4.2 2D Fourier Transform Imaging 21

2.5 Conventional MRI Hardware 22

2.5.1 Superconducting Magnets for B_0 22

2.5.2 Permanent Magnets for B_0 22

2.5.3 Control Console and Signal Chain 24

3 Spokes-and-Hub Magnet **27**

3.1 Magnet Design Considerations 27

3.2 Magnetic Field Simulation and Optimization 28

3.3 Magnet Construction 30

3.4 Field Measurements 33

4 Results **35**

4.1 Magnet Characterization 35

4.1.1 Imaging Slice Thickness 35
4.1.2 Radially Symmetric Fields 37
4.1.3 Field Measurements 37
4.2 Spin Echoes 39

5 Conclusions **43**

List of Figures

1-1 Existing low-field, permanent magnet MR systems. (a) tabletop educational scanner from [3] (b) single-sided Halbach hydration sensor from [4] (c) MR cap from [5] (d) rotating Halbach array MRI system from [6, 7] (e) ultra-low field SQUID-based MRI system from [8, 9] (f) FDA-approved, portable point-of-care scanner from [10] 15

2-1 Proton spin evolution in the presence of B_0 and B_1 fields. (a) proton rotating about its own axis in the absence of an external magnetic field (b) proton precession at the Larmor frequency when exposed to a z-directed external magnetic field, B_0 (c) in the laboratory frame of reference, RF pulse that is tuned to Larmor frequency is applied to the transverse plane as the magnetization moves away from the z-axis (d) simplified rotating frame of reference showing flip angle, θ, of the magnetization vector when RF pulse is applied 19

2-2 Conventional spin echo sequence for 2D discrete Fourier image encoding 21

2-3 Halbach cylinder permanent magnet designs from Wald et al. [1] . . . 23

2-4 Radially magnetized rings of magnets adapted from [25] 23

2-5 NMR/MRI consoles: (from left to right) Tecmag Apollo (35,000 USD) [29], Medusa (2,000 USD) [30], Red Pitaya (400 USD) [31] 25

3-1 Simulated B_0 field maps in x-y (top row) and y-z plane (bottom row) 29

3-2 Hub separation distance optimization 29

3-3 STL model of 3D printed magnet enclosure 30

3-4 Assembled spokes-and-hub magnets with simulated B_0 field and homogeneity. In each row, from left to right: picture of assembled magnet; quadrature points for field simulator; simulated x-y fields through center slice of magnet; field homogeneity along one radius within center slice 31
3-5 Array of ALS31300 Hall effect sensors for B_0 field measurements . . . 33

4-1 Simulated imaging slice thickness for 0.25, 1, and 2 mm slabs. Top row: ΔB_0 field map of entire slice; Bottom row: ΔB_0 along a single radius of the slice 36
4-2 B_0 field along rings at different radii in the desired FOV 37
4-3 B_0 field measurements along one radius of spokes-and-hub magnets . 38
4-4 RF signal chain 40
4-5 (a) Received signal chain circuit schematic using THS4222 op-amp (b) PCB layout for 8-channel STHV800 ultrasound driver chip and receive signal chain 40
4-6 At-home spokes-and-hub MR setup 41
4-7 Spin echoes on spokes-and-hub magnets 42

List of Tables

3.1 Constructed spokes-and-hub magnets 32

4.1 ΔB_0 and excitation frequency for various simulated slice thicknesses . 36

Chapter 1

Introduction

Magnetic resonance imaging (MRI) is considered by many as the gold standard imaging diagnostic tool in clinical settings. It is both very safe and a remarkably revealing tool in high-end hospital care. However, access to MRI is limited in point-of-care detection and diagnostics as well as in its educational use due to the cost, size, and safety of superconducting magnets. In this thesis, I am proposing a novel, easy-to-assemble "spokes-and-hub" magnet design for low-field (ten to hundreds of mT) portable scanners that employs lost-cost and readily-accessible components. To design this magnet, fields from bar magnets are computed efficiently by differentiating the potential from end-cap equivalent charges thus allowing for computationally-optimized field uniformity. Existing ultrasound-capable ICs will then be leveraged with classical MR imaging strategies to create a low-cost, portable imager.

1.1 Low-Cost, Portable MRI

Following in the footsteps of other powerful imaging modalities, such as computed tomography (CT), ultrasound, and x-ray, there has been increased focus on development of portable scanners in the MR community [1, 2]. While portable x-ray and ultrasound systems have been used in point-of-care applications since the early 1900s, it wasn't until recent decline in the cost of manufacturing rare-earth permanent magnets and embedded systems/microcontrollers that has led to rapid development of low-field, low-cost, portable MRI systems.

Within the field of MR, many of the advancements in portable imagers have been led by groups in the Greater Boston area at MIT and the MGH Martino's Center for Biomedical Imaging, several of whom I've been able to work with and learn from (Fig. 1-1). At MIT/MGH, low-cost portable MR tools for a variety of use cases have been developed, from tabletop educational scanners (Fig. 1-1a) to single-sided MR hydration sensors (Fig. 1-1b) to point-of-care brain imagers (Fig. 1-1c,d) [3, 4, 5, 6, 7]. In addition, other research groups and industry startups have explored the low-field MR space—the ultra-low-field SQUID-based system from Los Alamos National Laboratory (Fig. 1-1e) and the portable, point-of-care scanner from the startup Hyperfine (Fig. 1-1f), to name a few [8, 9, 10, 11].

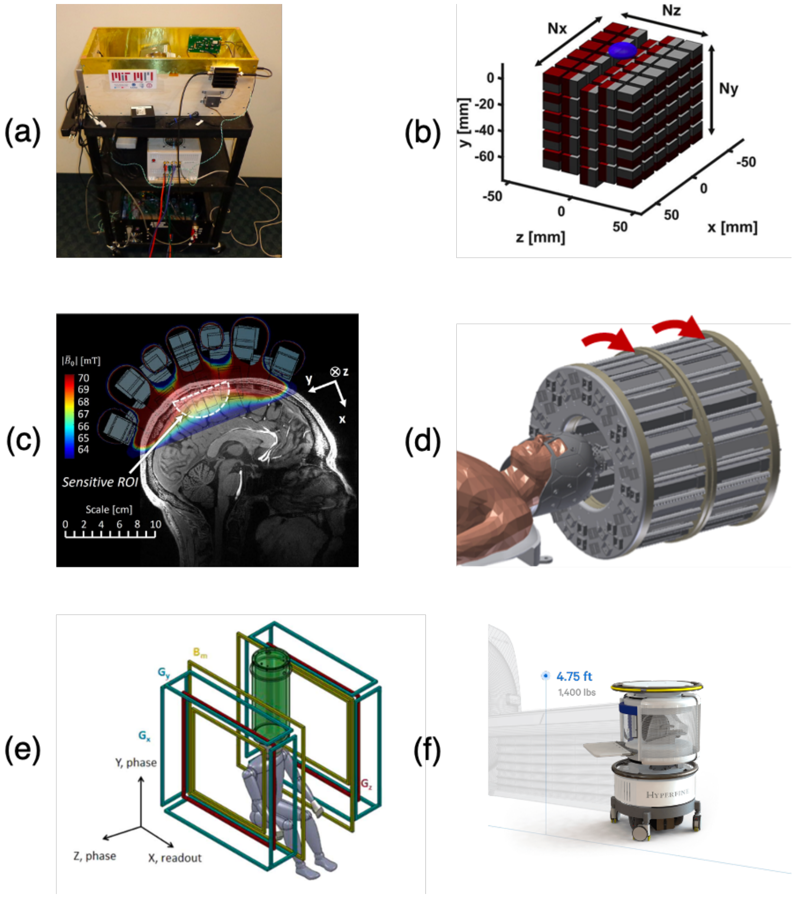
(a)
(b)
Nx
Nz
Ny
y [mm]
0
-20
-40
-60
-50
0
50
z [mm]
-50
0
50
x [mm]
(c)
|B0| [mT]
70
69
68
67
66
65
64
y
⊗z
x
Sensitive ROI
Scale [cm]
0 2 4 6 8 10
(d)
(e)
Bm
Gy
Gx
Gz
Y, phase
Z, phase
X, readout
(f)
4.75 ft
1,400 lbs
HYPERFINE

Figure 1-1: Existing low-field, permanent magnet MR systems. (a) tabletop educational scanner from [3] (b) single-sided Halbach hydration sensor from [4] (c) MR cap from [5] (d) rotating Halbach array MRI system from [6, 7] (e) ultra-low field SQUID-based MRI system from [8, 9] (f) FDA-approved, portable point-of-care scanner from [10]

Chapter 2

MRI Background

Since its discovery in the early 1970s, magnetic resonance imaging (MRI) has provided noninvasive diagnostic imaging of the human anatomy. Some advantages of MR include no ionizing radiation, high spatial resolution, and a large range of physical parameters that can be captured. However, conventional MR hardware is expensive and often limited in accessibility outside of hospital settings [1].

MR scanners utilize static and alternating radiofrequency (RF) magnetic fields to excite hydrogen atoms (protons) which are abundant in the body, most notably in water and fat. When subjected to a strong external magnetic field, B_0, the magnetic moment vectors of the hydrogen atoms align in the direction of the field and exhibit a resonance at the Larmor frequency, f_0.

$$f_0 = \frac{\gamma}{2\pi} \mid B_0 \mid \tag{2.1}$$

γ is referred to as the gyromagnetic ratio of a particle's magnetic moment to its angular momentum. Hydrogen atoms in an external magnetic field will precess at a frequency that is proportional to the applied field and $\frac{\gamma}{2\pi} = 42.577$ MHz/T. MR convention dictates that the external field is z-directed, or longitudinally-directed [12].

2.1 Main Magnetic Field (B_0)

In MR, a strong magnet produces a static magnetic field (B_0) in the z-direction. For clinical scanners, the B_0 field typically ranges from 1.5 - 7 Tesla. These magnets are passively shimmed using small pieces of metal or magnets to be homogeneous to around ≤ 1 part per million (ppm). When a proton is exposed to a B_0 field, a z-directed net magnitization, M_0, is induced on it, and they will precess in the B_0 field at the Larmor frequency [12].

2.2 Radiofrequency (RF) Excitation (B_1)

In order to obtain an MR signal, an RF pulse is applied to a coil in the x-y plane (or transverse-plane) to excite the spins of the hydrogen atoms into resonance. This RF pulse is referred to as the B_1 field and oscillates at the Larmor frequency of the static B_0 field (Fig. 2-1). The B_1 field rotates the proton magnetization by an angle that is a function of its strength (B_1) and duration (τ).

$$\theta = \gamma B_1 \tau \tag{2.2}$$

In a typical MR system, the B_1 field is several orders of magnitude smaller than B_0 and its duration is on the order of milliseconds. The RF transmit coil generally consists of one or more turns of wire placed within the main B_0 magnet.

Similarly, an RF coil is also responsible for receiving the MR signal from the excited spins. This signal is captured in the induced voltage on the coil due to a change in magnetic flux as defined in Faraday's law of induction.

$$\mathcal{E} = -\frac{d\phi_B}{dt} \tag{2.3}$$

In nuclear magnetic resonance (NMR) and MRI, the nuclear magnetization vector is governed by the Bloch equations:

$$\frac{d\boldsymbol{M}}{dt} = \boldsymbol{M} \times \gamma \boldsymbol{B} - \frac{M_x i + M_y j}{T_2} - \frac{(M_z - M_0)k}{T_1} \tag{2.4}$$

where T_1 represents the time constant for return of M_z and T_2 represents the decay of the transverse magnetizations, M_x and My.

Oftentimes, a single coil performs both RF transmit and receive (T/R). Arrays of T/R coils are also common in clinical MR, but will not be discussed here (see [13, 14]). After RF excitation, there is a time-varying signal called the free induction decay (FID) that results from the decaying transverse magnetization (M_{xy}). Sets of FIDs and refocused FIDs can be reconstructed into an MR image [15].

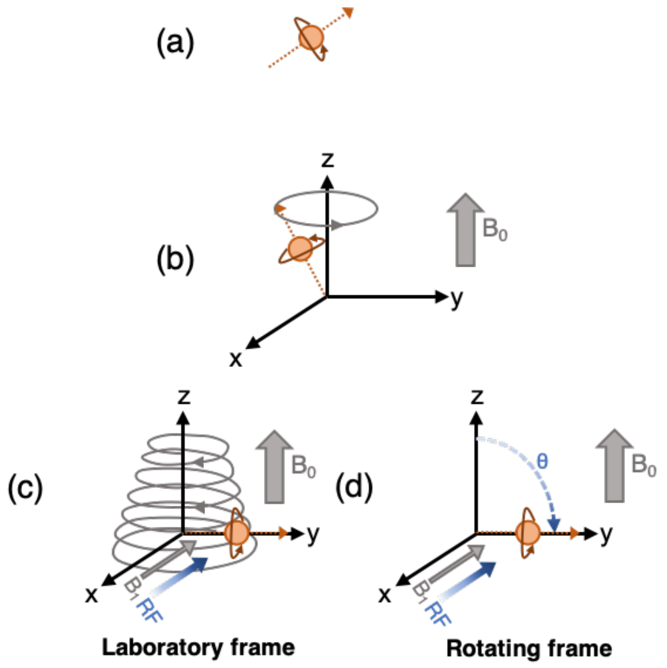

Figure 2-1: Proton spin evolution in the presence of B_0 and B_1 fields. (a) proton rotating about its own axis in the absence of an external magnetic field (b) proton precession at the Larmor frequency when exposed to a z-directed external magnetic field, B_0 (c) in the laboratory frame of reference, RF pulse that is tuned to Larmor frequency is applied to the transverse plane as the magnetization moves away from the z-axis (d) simplified rotating frame of reference showing flip angle, θ, of the magnetization vector when RF pulse is applied

2.3 Gradient Fields

Conventional MR imaging relies on linear, DC, spatial encoding magnetic fields in the x-, y-, and z-directions. These fields, referred to as the gradient fields (G_x, G_y, and

G_z), are turned on and off during the image acquisition process. The gradients allow for spatial localization of received signals by perturbing the B_0 homogeneity. Depending on the desired orientation of the imaging plane, each gradient axis corresponds to either a slice-select, phase-encoding, or frequency-encoding/readout gradient. A typical clinical MR gradient strength is less than 1 G/cm or 10 mT/m.

2.4 Signal Acquisition

Two basic image acquisition methods are most commonly used low-field MRI: projection-based reconstruction and 2D Fourier transform imaging with linear gradients described above. However, there are dozens of more sophisticated image acquisition schemes that have been employed in clinical MR imaging that will not be discussed here.

For both projection and Fourier imaging, a 90° excitation and 180° refocusing pulse in the B_1 transverse axis are played in succession, separated by some time, TE/2. At some time after the initial 90° pulse, the echo time (TE), the excited spins are back in phase and produce what is known as the spin echo (SE) signal that is picked up by the RF receive coil.

2.4.1 Projection-Based Reconstruction

Similar to the tomographic projection techniques used in x-ray and CT, early MR and NMR imaging made use of this method by collecting projections of magnetization vector signals along several different angles in the presence of some gradient field and integrating over the excited plane [16, 17, 18, 19]. The total received signal $s_r(t)$ is given by

$$s_r(t) = \int_x \int_y m(x,y) e^{-j\omega_0 t} e^{-j\gamma G_x t} dx dy \tag{2.5}$$

The baseband signal is then given by

$$s(t) = s_r(t)e^{+j\omega_0 t} \tag{2.6}$$

2.4.2 2D Fourier Transform Imaging

Most commonly used in MRI is the 2D Fourier transform approach where many projections are taken at one single projection angle to reconstruct an image, m(x,y). Conventional MR acquisition involves using linear gradient waveforms (see Section 2.3) multiplied by a set spatial frequency weighting factor to sample in the Cartesian frequency domain, called k-space. When the prescribed set of k-space lines are sampled, an image can be reconstructed using the 2D discrete Fourier transform (DFT). The acquisition timing diagram for the 2DFT is shown in Fig. 2-2.

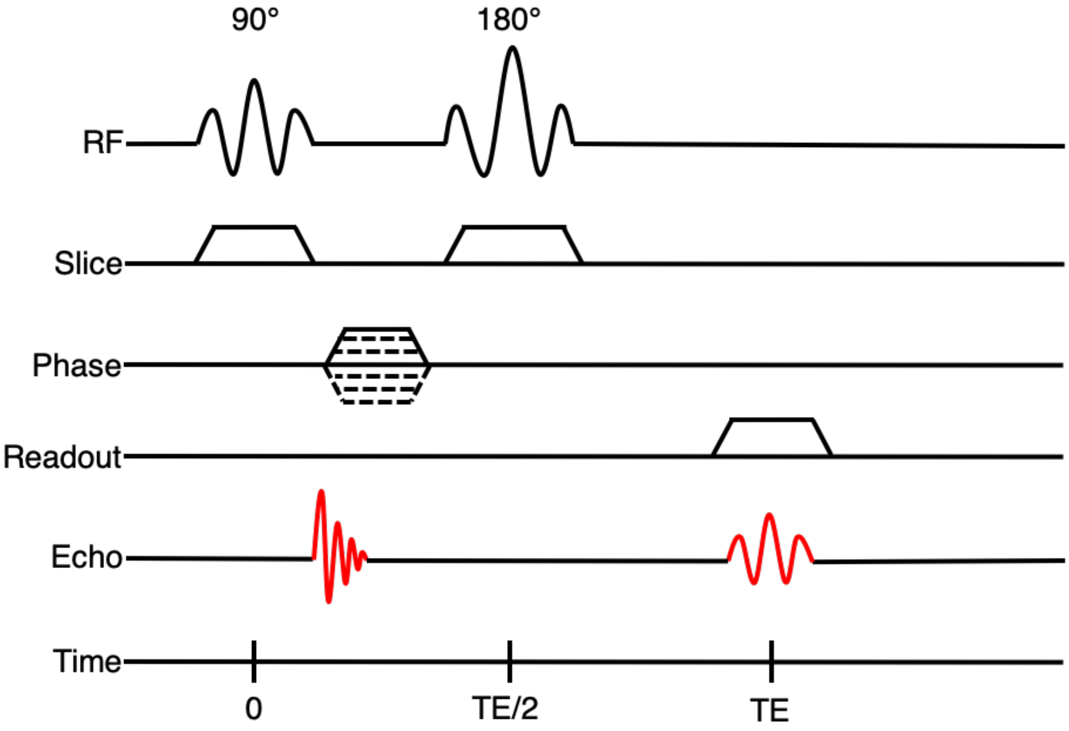

Figure 2-2: Conventional spin echo sequence for 2D discrete Fourier image encoding

2.5 Conventional MRI Hardware

2.5.1 Superconducting Magnets for B_0

Most clinical magnets are superconducting solenoidal electromagnets whose coils are cooled in liquid helium to maintain a homogeneous B_0 field. While these magnets are very homogeneous and can provide high-resolution imaging, the cost of purchasing and maintaining the magnet remain very high. Typical 1.5T and 3T clinical magnets cost an average of 1.5 and 2 million US dollars (USD), respectively [20]. On top of this base cost, there are also significant costs to maintaining the sitting cost of the cryogenic cooling system as well as building an RF-shielded room, which can amount to as much as 100,000 USD [1].

2.5.2 Permanent Magnets for B_0

Since the introduction of NdFeB rare-earth magnets in the 1980s, permanent magnet arrays for low-field B_0 magnets has becoming increasingly popular as a means for reducing hardware costs (in both the magnet and RF subsystem) [21]. A popular configuration that has been explored comes from the work of Halbach [22, 23, 24]. Various permanent magnet Halbach cylinder designs have been discussed in a recent review article by Wald et al. and are shown in Fig. 2-3 [1]. Several Halbach array MR systems that have been built are also found in Fig. 1-1.

Another permanent magnet topology that has been proposed for low-field MR comes from a 1991 patent by Aubert that involves using radially polarized ring magnets or NdFeB cube magnets arranged in a ring to create a longitudinal magnetic field (whereas the Halbach array has a transverse field) [25, 26, 27, 28]. This magnet topology provides opportunities to explore novel image encoding strategies and coil geometries in a low-cost system; however, it has yet to be built in a physical system and the current optimization methods for designing these magnets are inefficient and computationally expensive as they integrate the fields over the entire surface of the ring. The focus of this thesis will discuss the optimization and construction of a MR permanent magnet topology similar to this design as well as a low-cost method for acquiring spin echoes from the magnet.

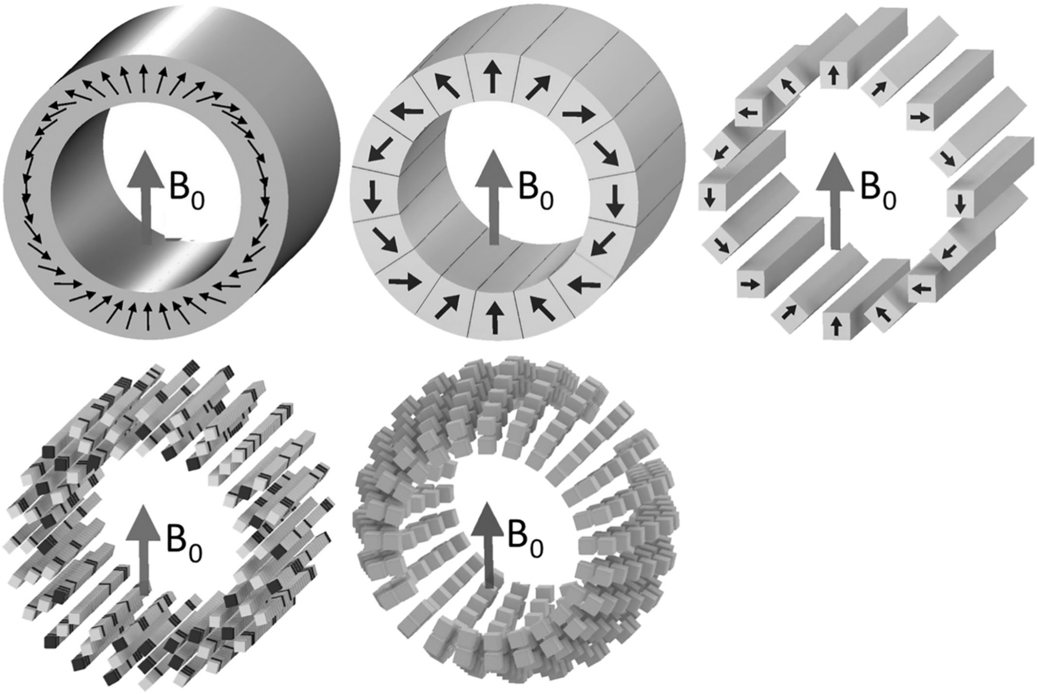

Figure 2-3: Halbach cylinder permanent magnet designs from Wald et al. [1]

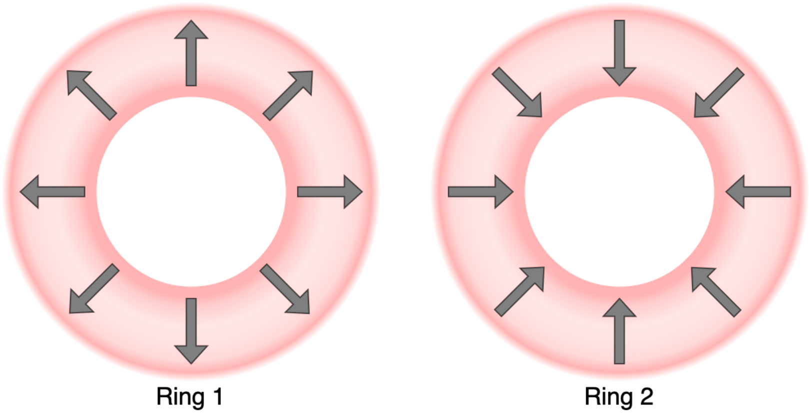

Figure 2-4: Radially magnetized rings of magnets adapted from [25]

2.5.3 Control Console and Signal Chain

In MR, the control console is responsible for controlling the timing and execution of RF and gradient pulse sequences, reads in the received signals, and sometimes even performs signal processing (e.g. down-conversion, filtering).

Conventional console systems from large MRI vendors like Siemens, GE, and Philips are available at a high cost due to its infrequent and nonrecurring development costs and low production volume. Commercially-available, programmable systems, such as the Redstone and Apollo NMR/MRI consoles from Tecmag, have been used in portable MR research but at a high cost (35,000 USD) [29, 5]. A handful of less-expensive (2,000-10,000 USD) MRI consoles have been developed in recent years to mitigate these costs, however, these systems are often closed-source and inflexible. The Medusa MR console from Stanford University (2011) is a well-known, scalable, modular USB-controlled solution for tabletop MR systems. However, it has limited memory for data and pulse sequence storage and is not phase stable between repetitions [30].

Particularly in the low-field MR regime (1-10MHz), recent improvements in low-cost, phase-stable RF signal processing modules are beginning to be exploited. For example, the Red Pitaya (400 USD) is a two-channel field programmable gate array (FPGA) capable of signal generation and digitization up to 40MHz [31]. The console systems mentioned here are shown in Fig. 2-5.

Since typical MR systems operate at a Larmor frequency above 50 MHz, they require high frequency RF amplifiers and preamplifiers for excitation and receive, respectively. This hardware often requires high power dissipation capabilities and strict bandwidth limits, driving up their cost. For low-field MR, RF amplifiers and preamplifiers can be obtained at a significantly lower cost due to the lessened frequency and power constraints [32].

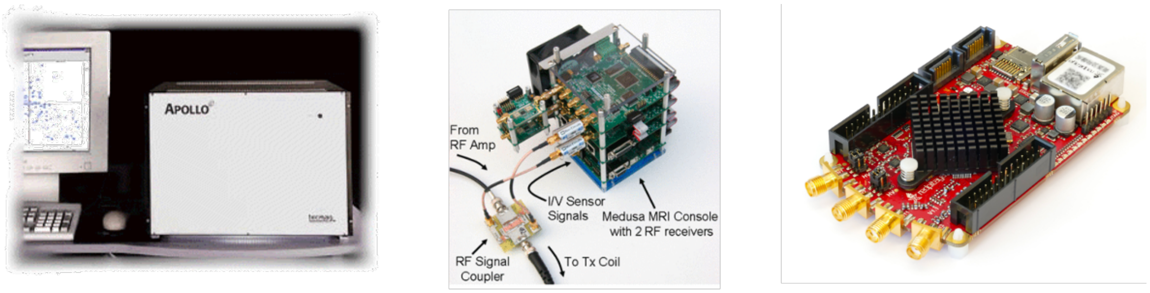
APOLLO
From RF Amp
I/V Sensor Signals
Medusa MRI Console with 2 RF receivers
RF Signal Coupler
To Tx Coil

Tecmag Apollo **Medusa** **Red Pitaya**

Figure 2-5: NMR/MRI consoles: (from left to right) Tecmag Apollo (35,000 USD) [29], Medusa (2,000 USD) [30], Red Pitaya (400 USD) [31]

Chapter 3

Spokes-and-Hub Magnet

3.1 Magnet Design Considerations

Other groups have demonstrated through calculation and simulation that sets of radially polarized ring magnets can create homogeneous fields as shown in Fig. 2-4 [25, 26, 27, 28]. To maintain a radial $\overrightarrow{B}$ field such that $\nabla \cdot \overrightarrow{B} = 0$, the magnetization density of the magnets must be manufactured to decrease continuously with radius. For this reason, these radially polarized magnets are expensive, difficult to manufacture uniformly, and dangerous to handle.

To mitigate these costs, I have proposed a "spokes-and-hub" magnet topology consisting of rings of cheap, commercially-available, and uniform axially polarized cylindrical/rectangular bar magnets, or "spokes". By calculating the fields from equivalent charges at the end points of the bar magnet spokes, the charges at the outer edge of the ring are negligible if the spokes are long enough. Because of the variety of commercial bar magnets geometries, the "hubs" can be densely packed as if it were a continuous ring to allow for uniform magnetic fields. Optimized spokes-and-hub magnets also have several advantages for hand-held, low-cost, low-field, single-slice MR imaging (50-200 mT) in that their frame is open, and they are safe to assemble, and can be scaled to different sizes and field strengths for both clinical and educational applications.

3.2 Magnetic Field Simulation and Optimization

Gauss-Legendre-quadrature based discretization of the equivalent-charge method was used to compute magnetic fields from axially-magnetized, cylindrical and square rods arranged in two large rings with opposite polarity (Fig. 3-1). Because the fields are so efficiently computed, optimization techniques can be used to quickly tune parameters for magnet design. Levenberg-Marquardt nonlinear least squares optimization in Matlab was used to minimize the field inhomogeneity about a desired field of view (FOV) at the center of the magnet, and obtain an optimal z-axis separation distance between the two sets of magnet rings. Differentiating the potential from end-cap equivalent charges is so efficient at computing fields from bar magnets, that in less than minute, a laptop running Matlab can computationally-optimize field uniformity in hundred-bar wagon-wheel (or spokes-and-hub) magnets [33, 34, 35, 36].

Shown in Fig. 3-1 can see examples of the simulated B_0 field through thin slices in the x-y and y-z planes at the center of an approximately 107 mT magnet. A noteworthy feature of these spokes-and-hub magnets is their field uniformity within slices in the x-y plane, with homogeneity on the order of hundreds of parts per million (ppm). Additionally, in this same simulated magnet, we can easily compute and analyze the B_0 field along other planes. The plot of B_0 in the y-z plane shows the field varies greatly (by around 1 mT, or 1000 ppm) over the same area as the x-y slice shown above it.

Because the B_0 homogeneity can be modified by adjusting the distance between rings, the hub separation that minimizes field inhomogeneities is optimized for in Matlab. Figure 3-2 demonstrates the B_0 field homogeneity for varying hub separations.

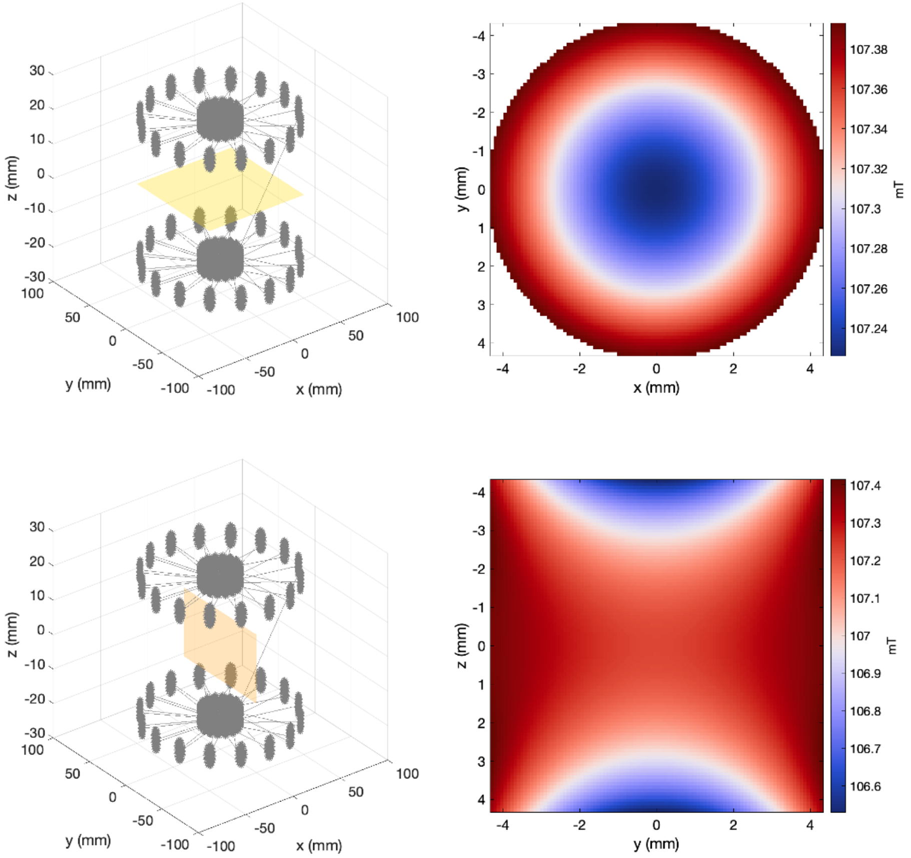

Figure 3-1: Simulated B_0 field maps in x-y (top row) and y-z plane (bottom row)

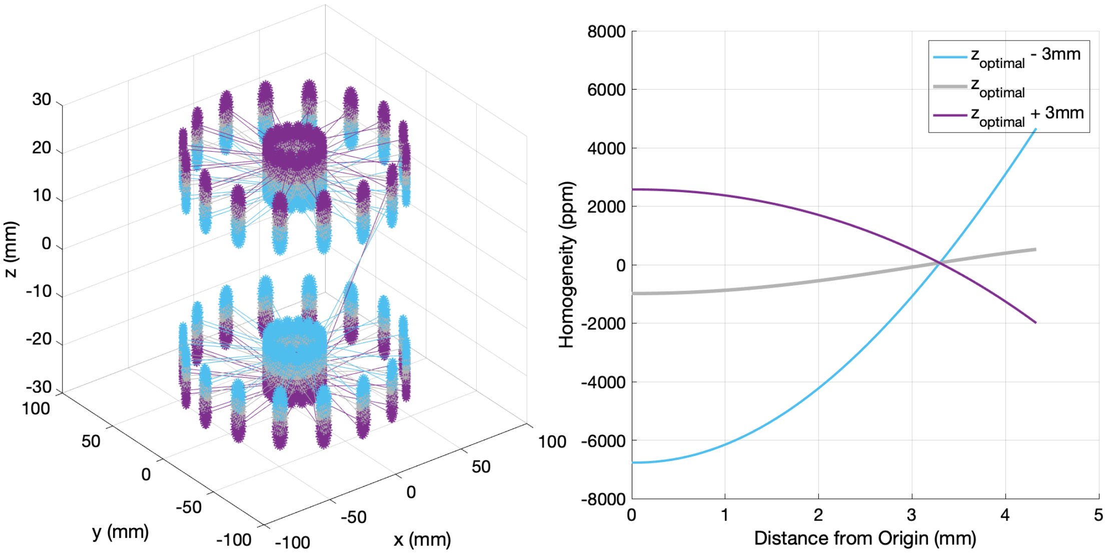

Figure 3-2: Hub separation distance optimization

3.3 Magnet Construction

The spokes-and-hub magnets can be assembled safely and quickly by sliding bar magnets into a 3D-printed enclosure (Fig. 3-3). The 3D printing process is easily reproducible even on budget PLA 3D printers because of the symmetry and simple geometry of the bar magnets. The magnets used were off-the-shelf axially-magnetized N42 magnets (K&J Magnetics, Plumsteadville, PA). This process can be easily customized for magnets of different sizes and field strengths. The openness of the 3D-printed frame allows for accessibility of the imaging plane from many different angles and orientations.

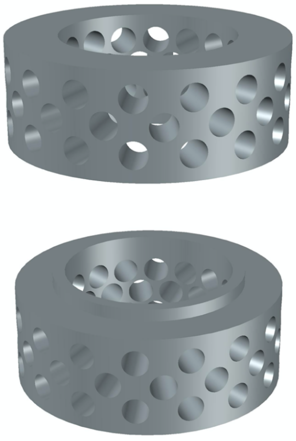

Figure 3-3: STL model of 3D printed magnet enclosure

From the Matlab field simulations (Fig. 3-4), I built spokes-and-hub magnets by arranging cylindrical- or square-shaped bar magnets into slots in 3D-printed enclosures. Four magnets with B_0 fields ranging from 54 to 190 mT were constructed. As shown in Table 3.1, they are low-cost, their frame is open, and are easily assembled and scaled, from finger to wrist to infant sized.

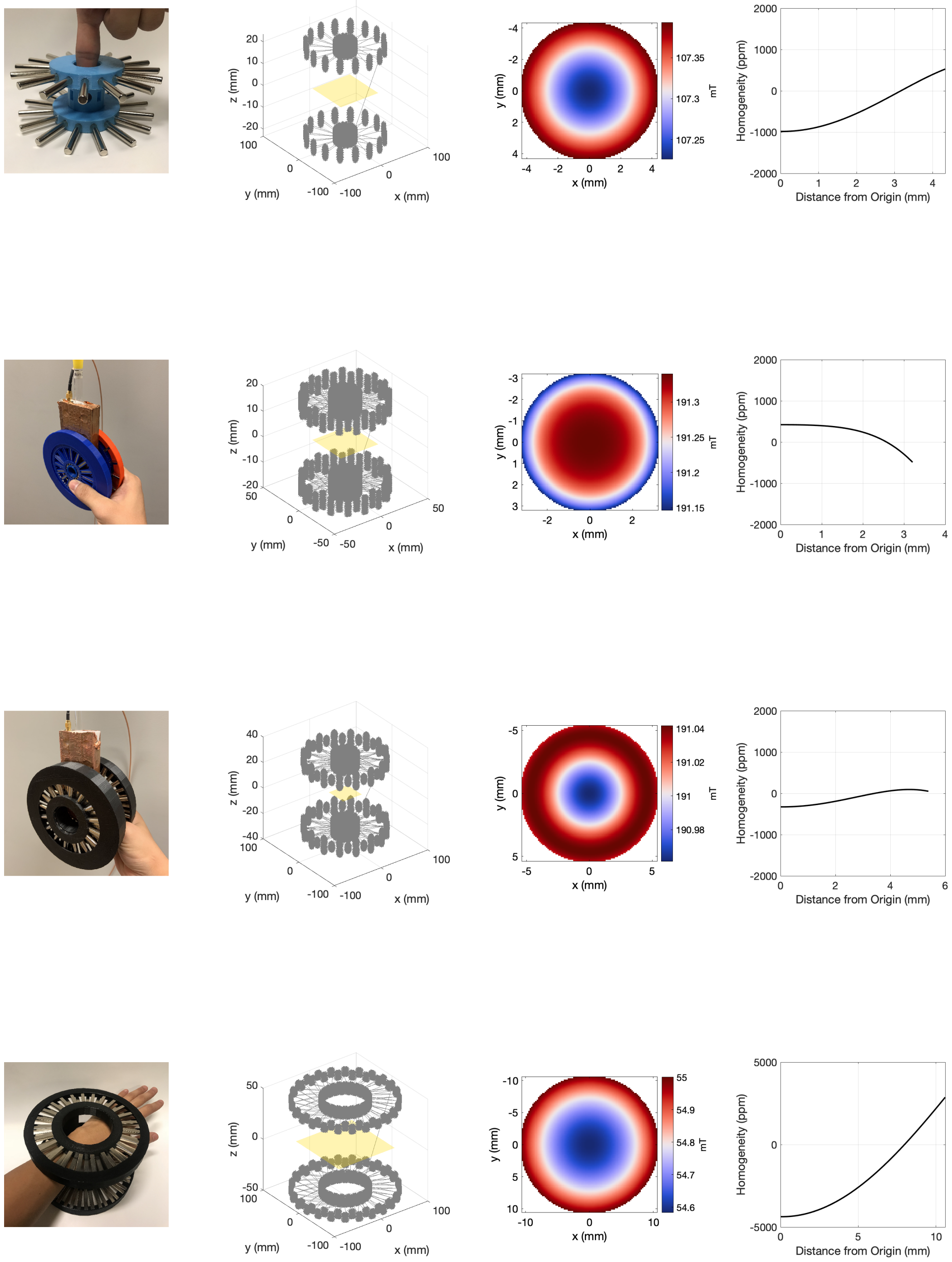

Figure 3-4: Assembled spokes-and-hub magnets with simulated B_0 field and homogeneity. In each row, from left to right: picture of assembled magnet; quadrature points for field simulator; simulated x-y fields through center slice of magnet; field homogeneity along one radius within center slice

Table 3.1: Constructed spokes-and-hub magnets

Magnet	Dimensions	Field Strength (Larmor frequency)	Cost
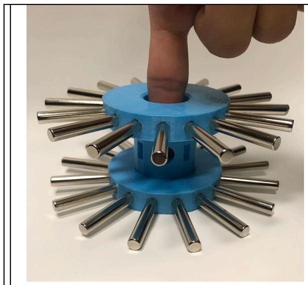	spokes: 32 cylindrical N42 magnets 6.35 mm diameter 50.8 mm length hub: 34.29 mm inner diameter	107 mT (4.57 MHz)	75 USD
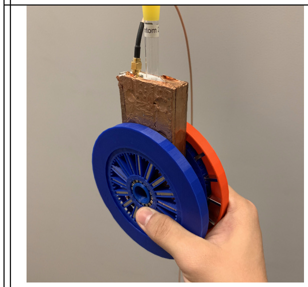	spokes: 192 rectangular N42 magnets 6.35 x 3.175 x 6.35 mm hub: 25.4 mm inner diameter	191.3 mT (8.145 MHz)	100 USD
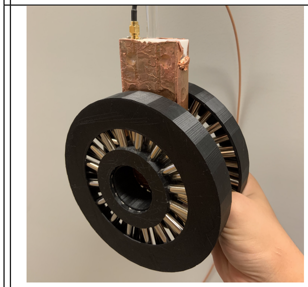	spokes: 96 cylindrical N42 magnets 6.35 mm diameter 50.8 mm length hub: 42.672 mm inner diameter	191.1 mT (8.137 MHz)	350 USD
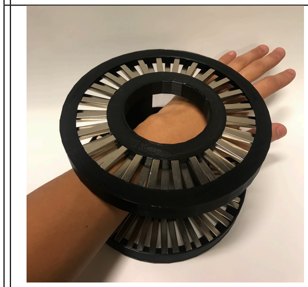	spokes: 96 rectangular N42 magnets 6.35 x 6.35 x 50.8 mm hub: 132.64 mm inner diameter	54.8 mT (2.33 MHz)	425 USD

3.4 Field Measurements

Since the z-directed field is assumed to be radially symmetric about the z = 0 plane, field measurements were taken along the inner radius of the magnet within the optimized FOV of interest using an ALS31300 3D Linear Hall-Effect Sensor (Allegro Microsystems, Manchester, NH).

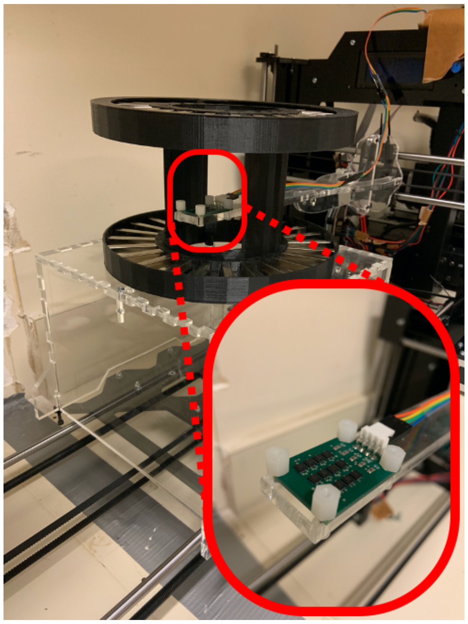

Figure 3-5: Array of ALS31300 Hall effect sensors for B_0 field measurements

Chapter 4

Results

4.1 Magnet Characterization

4.1.1 Imaging Slice Thickness

Looking into the feasible slice thicknesses for MR imaging, I've shown ΔB_0 maps in Fig. 4-1 for slice thickness of 0.25, 1, and 2 mm where the an inter-slice homogeneity ranges from tens to thousands of ppm. The ΔB_0 maps were calculated by subtracting the field at the center x-y plane between the hub rings from the an x-y slice 0.25, 1, and 2 mm away. Table 4.1 lists the maximum ΔB_0 found within each of the simulated slices and the corresponding frequency bandwidth that would be required from an RF pulse to excite the entire region. Because of the large variation in B_0 in the z-direction, we see that the spokes-and-hub magnets should be limited to very thin slices and cannot be used directly for volumetric imaging without implementing broadband RF pulses. Volumetric images instead can be obtained by sliding the magnet, as made possible by its open frame.

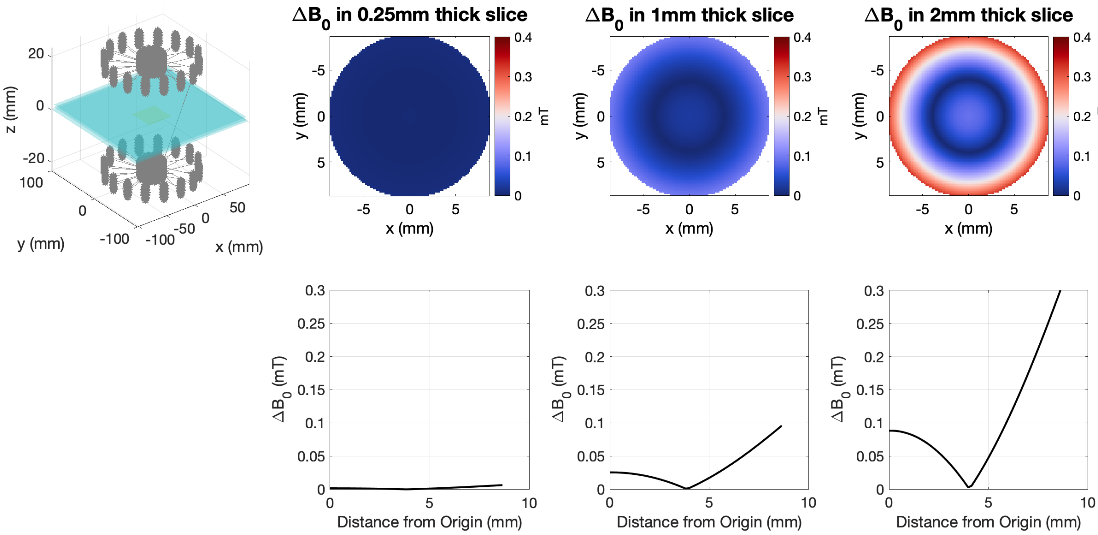

Figure 4-1: Simulated imaging slice thickness for 0.25, 1, and 2 mm slabs. Top row: ΔB_0 field map of entire slice; Bottom row: ΔB_0 along a single radius of the slice

Table 4.1: ΔB_0 and excitation frequency for various simulated slice thicknesses

Slice Thickness	Maximum ΔB_0	Required Excitation Frequency Bandwidth
0.25 mm	0.0064 mT	0.27 kHz
1 mm	0.0959 mT	4.08 kHz
2 mm	0.3026 mT	12.88 kHz

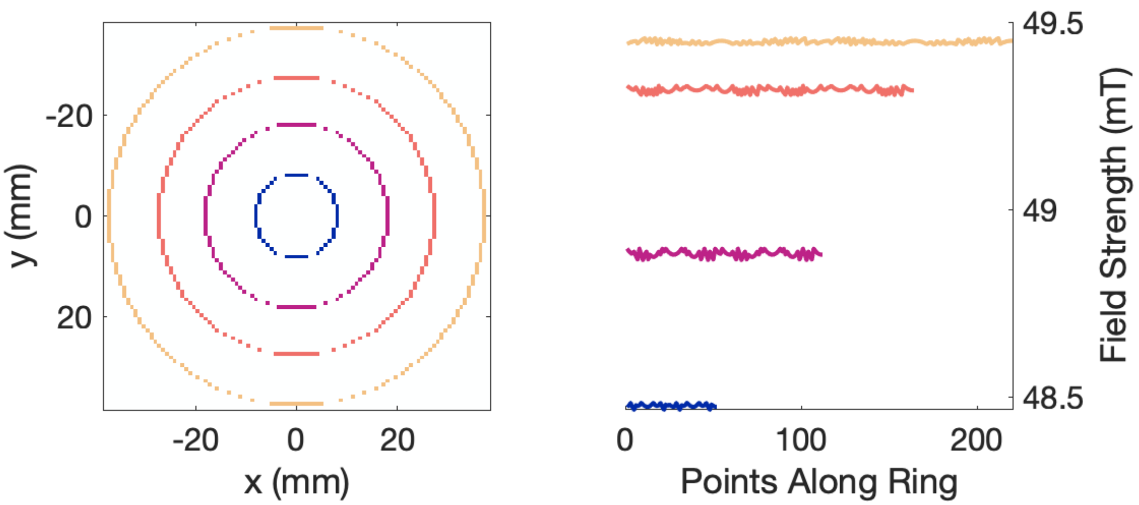

Figure 4-2: B_0 field along rings at different radii in the desired FOV

4.1.2 Radially Symmetric Fields

Furthermore, when looking into the field patterns along rings within the same thin slice, the fields are radially symmetric and have little variation within each ring compared to the homogeneity of the entire slice. As shown in Fig. 4-2, the field variation within the rings is less than 0.02 mT with a homogeneity within a couple ppm. The variation along each ring can be attributed to error when mapping the Cartesian discretization of simulation points to the circular mask for selecting rings of fields. This radial symmetry is noteworthy because it can be exploited for imaging or for projection-encoding.

4.1.3 Field Measurements

Because of the spokes-and-hub magnet's radial symmetry discussed above, field measurements were made along a single radius. The measured fields are shown by red circles and compared to simulated fields in white. The precision of the hall-effect probe is denote by the red error bars. Measured fields over the optimized FOV closely match the simulated B_0 within the hall-effect probe margin of error for each magnet.

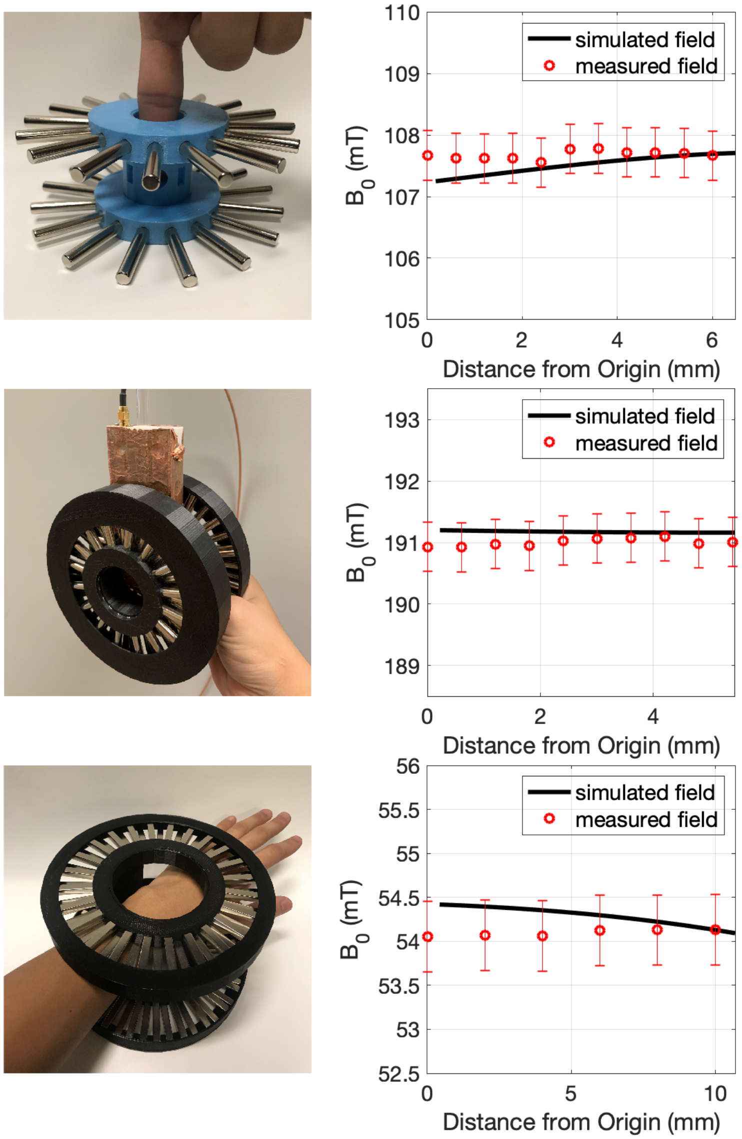

Figure 4-3: B_0 field measurements along one radius of spokes-and-hub magnets

4.2 Spin Echoes

To demonstrate the feasibility of these spokes-and-hub magnets as tools for MR imaging, I obtained spin echoes on the 191 mT magnets using the signal chain detailed in Fig. 4-4. The RF subsystem consists of a Teensy 4.0 microcontroller, an 8-channel STHV800 ultrasound pulser chip, and a transmit/receive coil. I used the STHV800 ultrasound pulser (30 USD, STMicroelectronics) to create programmable, high-voltage pulses as well as receiving low-amplitude signals through its T/R switch. Because each channel is driven by 2 digital bits, the chip can be enabled by digital square-wave outputs. Teensy 4.0 (20 USD, PJRC), with its ARM Cortex-M7 processor and dynamic clock scaling functionality, can generate reliable pulses with a timing resolution of 3.3 ns that the ultrasound pulser can drive the RF coil. This allows for careful control of the RF output from the Teensy through amplitude and frequency modulation. The low-amplitude MR signals received on the ultrasound driver are amplified through two inverting op-amp stages for a total gain of 100. I designed a printed circuit board (PCB) to control the STHV800 driver and receive signal chain, and the 4-layer board was prototyped by PCBWay (Shenzhen, China) shown in Fig. 4-5. The RF coil was taken from the MIT and Martinos Center tabletop educational scanners that also operate at the same Larmor frequency of ∼8.13MHz. The Teensy's ARM Cortex-M7 processor. The use of lower fields strengths allows for significantly lowered cost of RF transmit and receive hardware compared to conventional MR because high voltage H-bridge drivers and operational amplifiers can be used at this frequency. The widespread accessibility to these parts also allows for the spokes-and-hub MR setup to be replicated outside of the laboratory environment. Figure 4-6 shows the at-home working system (despite global pandemic conditions).

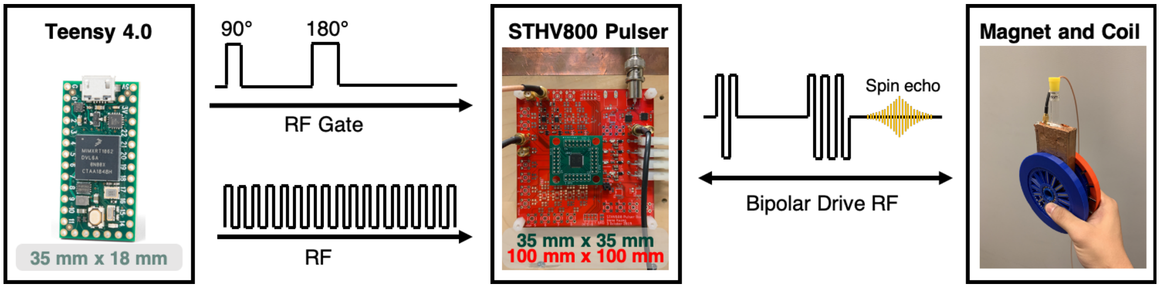
Teensy 4.0
35 mm x 18 mm
90°
180°
RF Gate
RF
STHV800 Pulser
35 mm x 35 mm
100 mm x 100 mm
Spin echo
Bipolar Drive RF
Magnet and Coil

Figure 4-4: RF signal chain

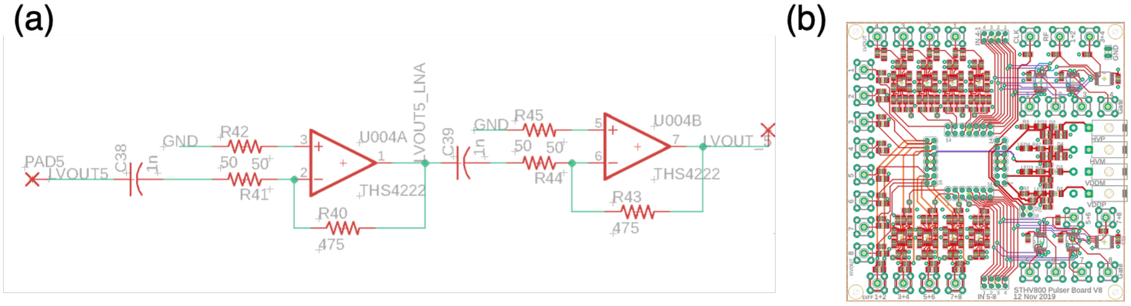
(a)
(b)
PAD5
LVOUT5
C38
1n
GND
R42
50
50
R41
3
2
U004A
1
THS4222
R40
475
VOUT5_LNA
C39
1n
GND
R45
50
50
R44
5
6
U004B
7
THS4222
LVOUT_5
R43
475
STHV800 Pulser Board V8
12 Nov 2019

Figure 4-5: (a) Received signal chain circuit schematic using THS4222 op-amp (b) PCB layout for 8-channel STHV800 ultrasound driver chip and receive signal chain

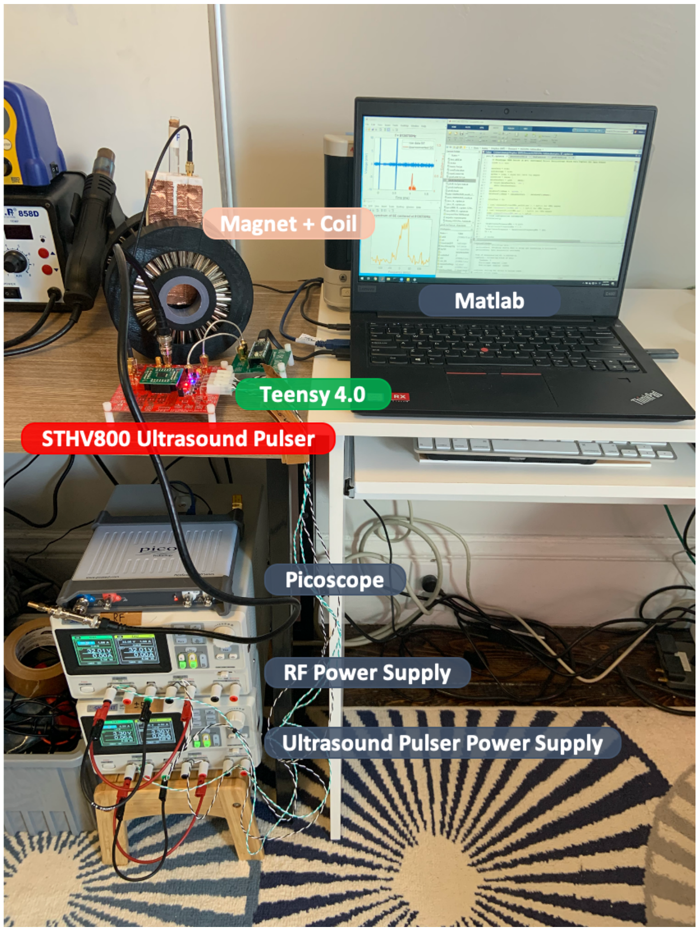
Magnet + Coil
Matlab
Teensy 4.0
STHV800 Ultrasound Pulser
Picoscope
RF Power Supply
Ultrasound Pulser Power Supply

Figure 4-6: At-home spokes-and-hub MR setup

Figure 4-7 presents spin echoes results obtained on both of the 191 mT spokes-and-hub magnets [37, 38]. A wideband 90 and 180° pulse was played in each spin echo sequence with an echo time of 0.5 ms. The spin echo signal was recorded on a low-cost (350 USD), USB-powered, PC oscilloscope, Picoscope 2206B (Pico Technology, Cambridgeshire, UK). Filtering and downconversion of the received spin echo to baseband was performed post-hoc in Matlab.

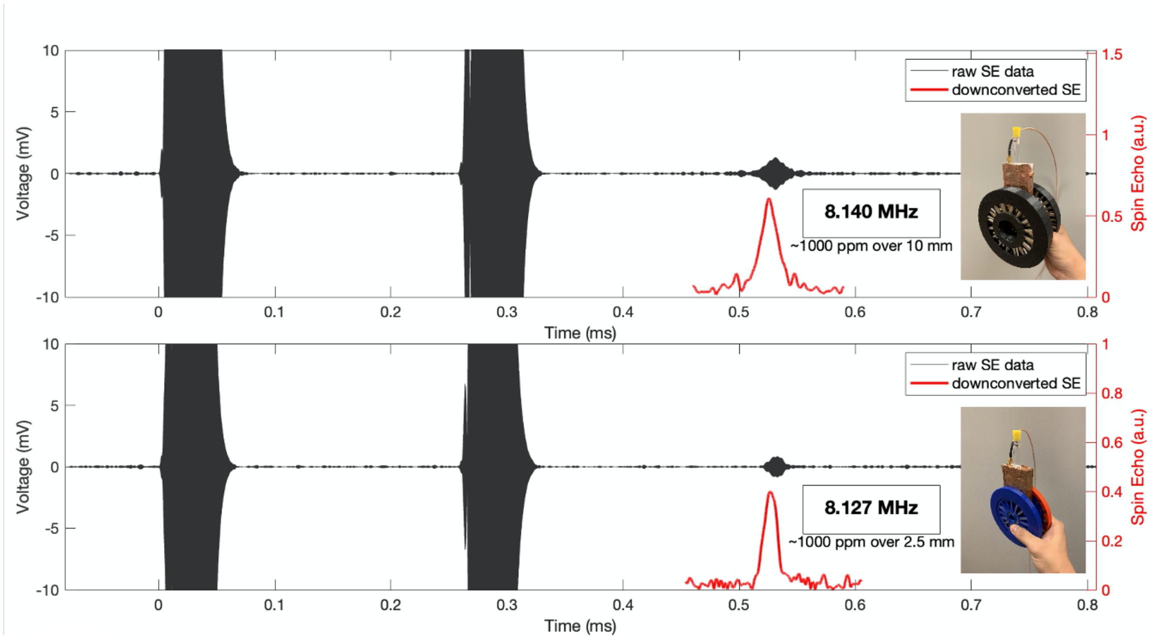

Figure 4-7: Spin echoes on spokes-and-hub magnets

Chapter 5

Conclusions

Here I have characterized and demonstrated feasibility of several, easy-to-assemble spokes-and-hub low-field permanent magnet structures for MRI. In simulation, we have a computationally-efficient method for accurately modeling the B0 field across multiple planes within the magnet bore. With the ability to efficiently simulate the fields, we can further optimize the fields within the magnet to also allow for built-in linear gradients in the static magnetic field by introducing unequal numbers of bar magnets within each ring. Regarding the design of the magnet, its open structure allows for imaging along all three axes, as well as potential for utilization of mechanical rotation of the magnet for gradient encoding and projection-based imaging [39, 6]. The spoke rings can also be easily taken apart to allow for novel coil geometries. Of particular interest, spokes-and-hub magnet demonstrates great promise as a low-cost, hand-held tool for clinical scanning of adult limbs/extremities and pediatric brains, most notably with applications towards hydrocephalus detection in newborns which does not require high-resolution imaging [40]. Moving forward, in my PhD, I plan to apply this spokes-and-hub topology to an imaging system capable of these clinical applications with fields optimized to capitalize on the magnet's inherent inhomogeneities.

Bibliography

[1] L. L. Wald, P. C. McDaniel, T. Witzel, J. P. Stockmann, and C. Z. Cooley, "Low-cost and portable MRI," *Journal of Magnetic Resonance Imaging*, pp. 1–11, 2019.

[2] J. P. Marques, F. F. Simonis, and A. G. Webb, "Low-field MRI: An MR physics perspective," *Journal of Magnetic Resonance Imaging*, vol. 49, no. 6, pp. 1528–1542, 2019.

[3] C. Z. Cooley, J. P. Stockmann, T. Witzel, C. LaPierre, A. Mareyam, F. Jia, M. Zaitsev, Y. Wenhui, W. Zheng, P. Stang, G. Scott, E. Adalsteinsson, J. K. White, and L. L. Wald, "Design and implementation of a low-cost, tabletop MRI scanner for education and research prototyping," *Journal of Magnetic Resonance*, vol. 310, p. 106625, 2020.

[4] A. Bashyam, M. Li, and M. J. Cima, "Design and experimental validation of Unilateral Linear Halbach magnet arrays for single-sided magnetic resonance," *Journal of Magnetic Resonance*, vol. 292, pp. 36–43, jul 2018.

[5] P. C. McDaniel, C. Z. Cooley, J. P. Stockmann, and L. L. Wald, "The MR Cap: A single-sided MRI system designed for potential point-of-care limited field-of-view brain imaging," *Magnetic Resonance in Medicine*, vol. 82, pp. 1946–1960, nov 2019.

[6] C. Z. Cooley, J. P. Stockmann, B. D. Armstrong, M. Sarracanie, M. H. Lev, M. S. Rosen, and L. L. Wald, "Two-dimensional imaging in a lightweight portable MRI scanner without gradient coils," *Magnetic Resonance in Medicine*, vol. 73, no. 2, pp. 872–883, 2015.

[7] C. Z. Cooley, M. W. Haskell, S. F. Cauley, C. Sappo, C. D. Lapierre, C. G. Ha, J. P. Stockmann, and L. L. Wald, "Design of sparse halbach magnet arrays for portable MRI using a genetic algorithm," *IEEE Transactions on Magnetics*, vol. 54, pp. 1–12, jan 2017.

[8] A. N. Matlashov, E. Burmistrov, P. E. Magnelind, L. Schultz, A. V. Urbaitis, P. L. Volegov, J. Yoder, and M. A. Espy, "SQUID-based systems for co-registration of ultra-low field nuclear magnetic resonance images and magnetoencephalography," *Physica C: Superconductivity and its Applications*, vol. 482, no. September 2014, pp. 19–26, 2012.

[9] M. A. Espy, P. E. Magnelind, A. N. Matlashov, S. G. Newman, H. J. Sandin, L. J. Schultz, R. Sedillo, A. V. Urbaitis, and P. L. Volegov, "Progress toward a deployable SQUID-based ultra-low field MRI system for anatomical imaging," *IEEE Transactions on Applied Superconductivity*, vol. 25, no. 3, 2015.

[10] M. S. Poole, C. Hugon, H. A. Dyvorne, L. Sacolick, W. J. Mileski, J. C. Jordan, A. B. Katze Jr, J. M. Rothberg, T. Rearick, and C. T. McNulty, "Portable magnetic resonance imaging methods and apparatus," 2018.

[11] V. S. Zotev, A. N. Matlachov, P. L. Volegov, H. J. Sandin, M. A. Espy, J. C. Mosher, A. V. Urbaitis, S. G. Newman, and R. H. Kraus, "Multi-Channel SQUID System for MEG and Ultra-Low-Field MRI," *IEEE Transactions on Applied Superconductivity*, vol. 17, no. 2, pp. 839–842, 2007.

[12] D. G. Nishimura, *Physical principles of magnetic resonance imaging.* Stanford University, 1996.

[13] B. Gruber, M. Froeling, T. Leiner, and D. W. Klomp, "RF coils: A practical guide for nonphysicists," *Journal of Magnetic Resonance Imaging*, vol. 48, no. 3, pp. 590–604, 2018.

[14] U. Katscher and P. Börnert, "Parallel RF transmission in MRI," *NMR in Biomedicine*, vol. 19, no. 3, pp. 393–400, 2006.

[15] R. H. Hashemi, W. G. Bradley, and C. J. Lisanti, *MRI: The Basics.* LWW, 3 ed., 2010.

[16] P. C. Lauterbur, "Image formation by induced local interactions: examples employing nuclear magnetic resonance," *Nature*, vol. 242, no. 5394, pp. 190–191, 1973.

[17] B. Liu, G. Wang, E. L. Ritman, G. Cao, J. Lu, O. Zhou, L. Zeng, and H. Yu, "Image reconstruction from limited angle projections collected by multisource interior x-ray imaging systems," *Physics in Medicine and Biology*, vol. 56, no. 19, pp. 6337–6357, 2011.

[18] J. E. Eben, T. L. Vent, C. J. Choi, S. Yarrabothula, L. Chai, M. Nolan, E. Kobe, R. J. Acciavatti, and A. D. A. Maidment, "Development of a next generation tomosynthesis system," *Proc. SPIE*, vol. 10573, no. March 2018, p. 212, 2018.

[19] G. Schultz, H. Weber, D. Gallichan, W. R. Witschey, A. M. Welz, C. A. Cocosco, J. Hennig, and M. Zaitsev, "Radial imaging with multipolar magnetic encoding fields," *IEEE Transactions on Medical Imaging*, vol. 30, no. 12, pp. 2134–2145, 2011.

[20] C. Obyn and I. Cleemput, "The capital cost and productivity of MRI in a Belgian setting," *Jbr-Btr*, vol. 93, no. 2, pp. 92–96, 2010.

[21] D. Brown, B. M. Ma, and Z. Chen, "Developments in the processing and properties of NdFeb-type permanent magnets," *Journal of Magnetism and Magnetic Materials*, vol. 248, no. 3, pp. 432–440, 2002.

[22] K. Halbach, "Design of permanent multipole magnets with oriented rare earth cobalt material," *Nuclear Instruments and Methods*, vol. 169, no. 1, pp. 1–10, 1980.

[23] G. Moresi and R. Magin, "Miniature permanent magnet for table-top NMR," *Concepts in Magnetic Resonance Part B: Magnetic Resonance Engineering*, vol. 19, no. 1, pp. 35–43, 2003.

[24] H. Raich and P. Blümler, "Design and construction of a dipolar Halbach array with a homogeneous field from identical bar magnets: NMR Mandhalas," *Concepts in Magnetic Resonance Part B: Magnetic Resonance Engineering*, vol. 23, no. 1, pp. 16–25, 2004.

[25] G. Aubert, "Cylindrical permanent magnet with longitudinal induced field," 1991.

[26] C. Hugon, F. D'Amico, G. Aubert, and D. Sakellariou, "Design of arbitrarily homogeneous permanent magnet systems for NMR and MRI: Theory and experimental developments of a simple portable magnet," *Journal of Magnetic Resonance*, vol. 205, no. 1, pp. 75–85, 2010.

[27] C. Hugon, P. M. Aguiar, G. Aubert, and D. Sakellariou, "Design, fabrication and evaluation of a low-cost homogeneous portable permanent magnet for NMR and MRI," *Comptes Rendus Chimie*, vol. 13, no. 4, pp. 388–393, 2010.

[28] Z. H. Ren, W. C. Mu, and S. Y. Huang, "Design and Optimization of a Ring-Pair Permanent Magnet Array for Head Imaging in a Low-Field Portable MRI System," *IEEE Transactions on Magnetics*, vol. 55, no. 1, pp. 1–8, 2019.

[29] Http://www.tecmag.com/history/, "History - Tecmag."

[30] P. P. Stang, S. M. Conolly, J. M. Santos, J. M. Pauly, and G. C. Scott, "Medusa: A scalable MR console using USB," *IEEE Transactions on Medical Imaging*, vol. 31, pp. 370–379, feb 2012.

[31] S. M. Anand, "OCRA : a low-cost, open-source FPGA-based MRI console capable of real-time control," Master's thesis, Massachusetts Institute of Technology, 2018.

[32] N. K. Almazrouei, M. I. Newton, and R. H. Morris, "Operational Amplifiers Revisited for Low Field Magnetic Resonance Relaxation Time Measurement Electronics," *Proceedings*, vol. 42, no. 1, p. 1, 2019.

[33] J. P. Selvaggi, S. Salon, O. M. Kwon, and M. V. Chari, “Calculating the external magnetic field from permanent magnets in permanent-magnet motors - An alternative method,” *IEEE Transactions on Magnetics*, vol. 40, no. 5, pp. 3278–3285, 2004.

[34] H. S. Choi, S. H. Lee, and I. H. Park, “General formulation of equivalent magnetic charge method for force density distribution on interface of different materials,” *IEEE Transactions on Magnetics*, vol. 41, no. 5, pp. 1420–1423, 2005.

[35] H. Rui and F. Jian, “Magnetic field analysis of permanent magnet array for planar motor based on Equivalent Magnetic Charge method,” *Proceedings of the World Congress on Intelligent Control and Automation (WCICA)*, pp. 3966–3970, 2012.

[36] M. Curti, J. J. Paulides, and E. A. Lomonova, “An overview of analytical methods for magnetic field computation,” *2015 10th International Conference on Ecological Vehicles and Renewable Energies, EVER 2015*, no. April, 2015.

[37] I. Kuang, N. Arango, J. Stockmann, E. Adalsteinsson, and J. White, “Equivalent-Charge-Based Optimization of Spokes-and-Hub Magnets for Hand-Held and Classroom MR Imaging,” in *Proc. Intl. Soc. Mag. Reson. Med. 27*, 2019.

[38] I. Kuang, N. Arango, J. Stockmann, E. Adalsteinsson, and J. White, “Bloch-Optimized Dithered-Ultrasound-Pulse RF for Low-Field Inhomogeneous Permanent Magnet MR Imagers,” *Proc. Intl. Soc. Mag. Reson. Med. 28*, 2020.

[39] Z. H. Cho, S. T. Chung, J. Y. Chung, S. H. Park, J. S. Kim, C. H. Moon, and I. K. Hong, “A new silent magnetic resonance imaging using a rotating DC gradient,” *Magnetic Resonance in Medicine*, vol. 39, no. 2, pp. 317–321, 1998.

[40] M. G. Kartal and O. Algin, “Evaluation of hydrocephalus and other cerebrospinal fluid disorders with MRI: An update,” *Insights into Imaging*, vol. 5, no. 4, pp. 531–541, 2014.